Supporting Information for

Exciton Delocalization Drives Rapid Singlet Fission in Nanoparticles of Acene Derivatives

Ryan D. Pensack,[1,†] Andrew J. Tilley,[1,†] Sean R. Parkin,[2] Tia S. Lee,[1] Marcia M. Payne,[2] Dong Gao,[1] Ashlee A. Jahnke,[1,‡] Daniel G. Oblinsky,[3] Peng-Fei Li,[1] John E. Anthony,[2,*] Dwight S. Seferos,[1,*] Gregory D. Scholes[1,3,*]

[1]Department of Chemistry, University of Toronto, Toronto, Ontario M5S 3H6, Canada,

[2]Department of Chemistry, University of Kentucky, Lexington, Kentucky 40506, United States,

[3]Department of Chemistry, Princeton University, Princeton, New Jersey 08544, United States

Additional synthetic details (hexacene derivatives)

The hexacene derivatives, 1,2,3,4-tetrafluoro-6,15-bis(tricyclopentylsilylethynyl)hexacene (F4-6,15-TCPS-Hn) and 1,2,3,4-tetrafluoro-7,14-bis(tricyclopentylsilylethynyl)hexacene (F4-7,14-TCPS-Hn), were synthesized as reported in the literature.[S1]

Additional experimental information (dynamic light scattering)

Dynamic light scattering measurements were performed on a Malvern Instruments Zetasizer Nano ZS instrument equipped with a Helium Neon laser (λ = 633 nm).

Additional experimental information (steady-state fluorescence spectroscopy)

Fluorimetry: Steady-state fluorescence measurements were performed on a PTI QuantaMaster 40-F NA spectrofluorometer (Photon Technology International, Inc., Birmingham, NJ) equipped with a Xenon lamp, double excitation monochromator, single emission monochromator, and a PTI Model 914 photomultiplier detection system. The PTI Model 914 photomultiplier detection system includes a Hamamatsu R928 photomultiplier tube. The grating in the emission monochromator was blazed at 400 nm with 1200 lines/mm spacing. Fluorescence emission spectra were corrected using calibration factors provided by the supplier; spectra were also corrected for background contributions by subtracting a measurement of the neat solvent. A photodiode was used to monitor and correct for run-time fluctuations in the light source intensity.

Fluorescence spectra of TIPS-Pn were recorded with the slit widths of both excitation and emission monochromators set to 1.00 mm. Typical scan parameters were 1 nm steps and at least 0.1 s integration time. The excitation wavelength varied with solvent, but was maintained within the range 590–610 nm. Fluorescence measurements were made on solutions with an optical density of 0.05 or less contained in a 1 cm pathlength quartz cell (Starna Cells, Inc., Atascadero, CA). The solutions were not degassed prior to the measurement.

Fluorescence quantum yield: Relative fluorescence quantum yield (FQY) measurements (Table S2). Typical scan parameters were 1 nm steps and 0.2 s integration time. At least six scans were obtained and averaged for measurements on the aqueous colloidal nanoparticle suspensions to increase the signal-to-noise. The sample solution was contained in a 1 cm pathlength quartz cell

(Starna Cells, Inc., Atascadero, CA) and the optical density was kept at or below 0.03 at the excitation wavelength. Oxazine-1 in ethanol (FQY = 0.14)[S2] was used as a relative FQY standard. Absolute ethanol (Commercial Alcohols) was used as the solvent for the dye; reagent-grade THF (Sigma-Aldrich) was used as a solvent for the Pn derivatives; distilled water was used as the dispersant for the nanoparticles. The excitation wavelength was set for 595 nm and remained unchanged between measurements on the dye solution, Pn derivative/THF solution, and aqueous colloidal nanoparticle suspensions to ensure an equivalent intensity of light was incident on the sample in each measurement. The slit widths were chosen to maximize the signal from the Pn derivative for measurements of the Pn derivative FQY or from the dye for measurements of the Pn derivative nanoparticle FQY while staying within the linear range of the detection system. Typical slit widths for both excitation and emission monochromators were 2.00 and 2.25 mm for measurements of the Pn derivative/THF and Pn derivative nanoparticle FQY, respectively. Sample solutions were de-oxygenated immediately prior to measurements by bubbling nitrogen gas through the solution for at least 15 minutes.

Additional experimental information (time-resolved spectroscopy)

Pump–probe spectroscopy: Femtosecond pump–probe measurements were performed on the same spectrometer reported in the main text. The sample was contained in a 1 mm path length spectrophotometer cell. Specific details regarding sample optical density and pump fluences are reported where appropriate.

Time-correlated singlet photon counting: Time-correlated singlet photon counting (TCSPC) measurements were made with excitation and emission wavelengths of 560 and 650 nm, respectively. The optical density of the sample at the maximum of the ^1L_a transition was ~0.1 and at the excitation wavelength was ~0.02. The sample was contained in a 1 cm fluorometer cell.

Additional experimental information (powder X-ray diffraction)

Aqueous dispersions of nanoparticles for powder X-ray diffraction experiments were prepared according to the procedure described in the main text until a total combined volume of ~500 mL had been reached. The combined aqueous nanoparticle suspensions were subsequently concentrated to a final volume of ~10 mL through rotary evaporation, with the remaining water removed by freeze drying (Thermo Fisher Scientific freeze dryer operated at −40 °C). Prior to freeze drying, absorption spectra were recorded to ensure that the nanoparticles had spectral features comparable to those used in the steady-state and pump–probe measurements. Powder diffraction data were obtained using a Rigaku MiniFlex 600 X-ray diffractometer with Cu K-alpha radiation (weighted average of Cu K-alpha1 and Cu K-alpha2; λ_{avg} = 1.54178 Å) and a NaI scintillation counter detector, typically within 72 hours of preparing the nanoparticle powder.

Additional theoretical details (Hartree-Fock calculation)

A pair of functionalized pentacene molecules was modelled using the Gaussian 09 software package.[S4] Hydrogen atoms were added and the alkyne groups were capped with methyl groups replacing the silicon atoms. The resulting structure underwent a restrained optimization freezing all atoms heavier than hydrogen using B3LYP/6-31G(d,p) level of theory.[S5-S7] The optimized monomeric structure was then subjected to a Hartree-Fock calculation using the 6-31G(d,p) basis set.[S8]

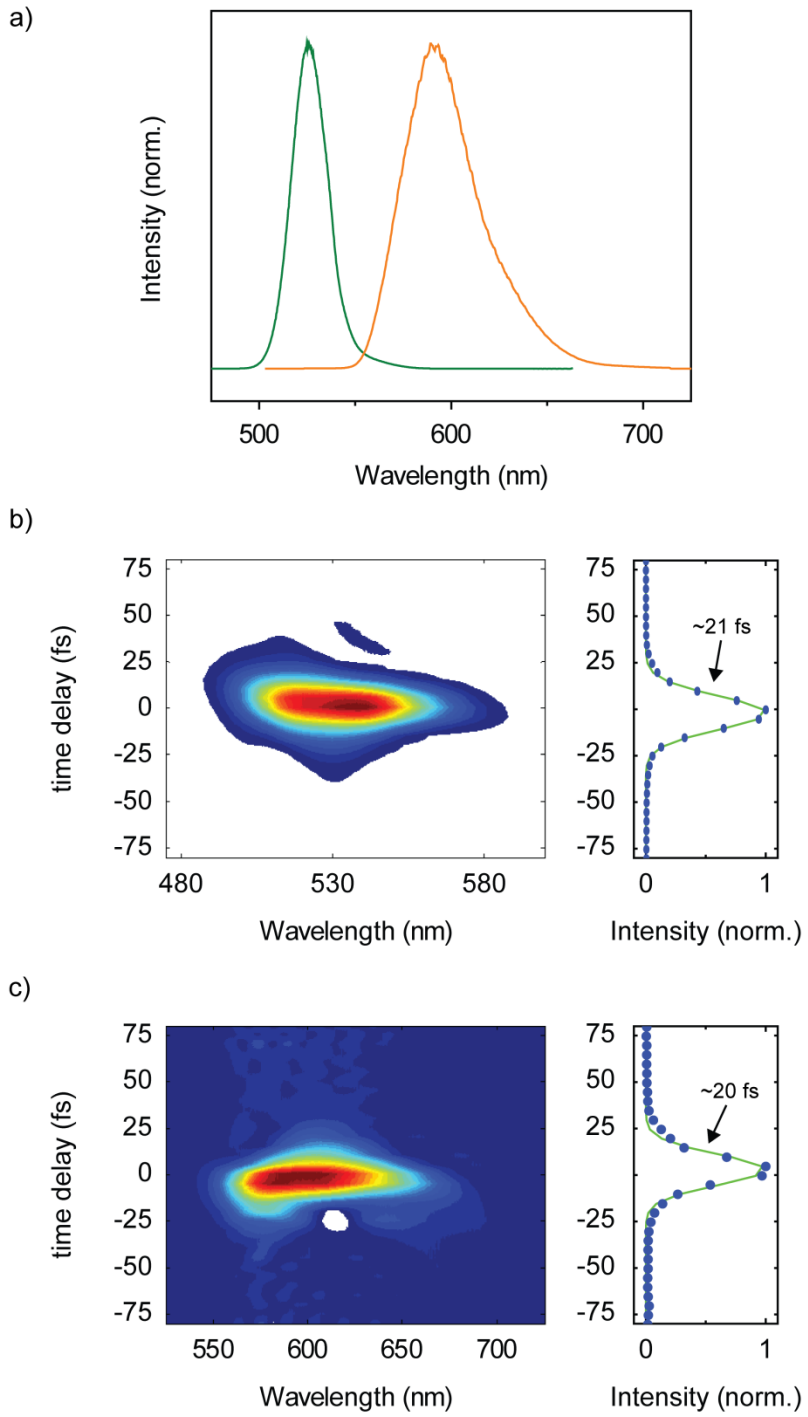

Figure S1. Typical NOPA spectra used for pump−probe experiments and associated representative pulse characterization. (a) Typical NOPA spectra encompassing the pentacene derivative singlet and triplet photoinduced absorptions (green) and singlet photoinduced

absorption and lowest-energy ground-state bleach features (orange). Polarization-gated frequency-resolved optical gating plots along with corresponding trace of the pulse duration (blue circles) and Gaussian fit (green line) for (b) green and (c) orange experiments. Pulse durations were typically ~21 and ~20 fs for the green and orange experiments, respectively.

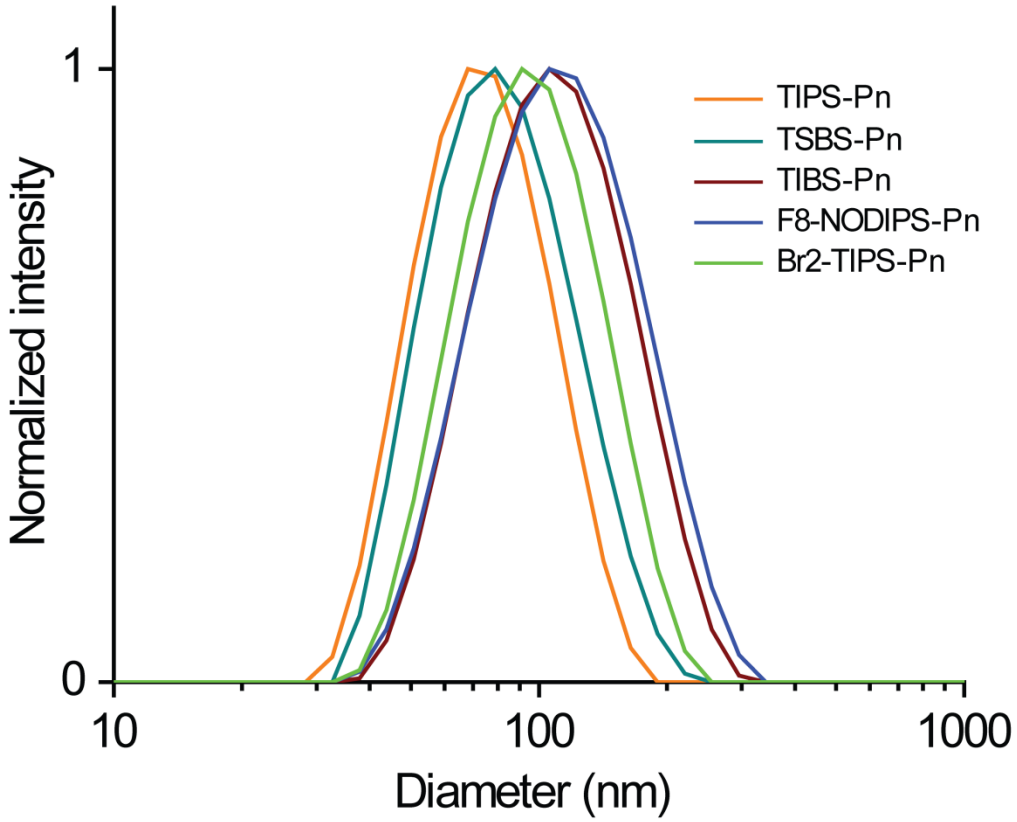

Figure S2. Results of dynamic light scattering measurements on aqueous colloidal TSBS-, TIPS-, TIBS-, F8-NODIPS-, and Br2-TIPS-pentacene nanoparticles. The measurements were performed at 25 °C. The Z-average values for each derivative are: TSBS- (76 nm), TIPS- (69 nm), TIBS- (94 nm), F8-NODIPS- (98 nm) and Br2-TIPS-Pn (81 nm).

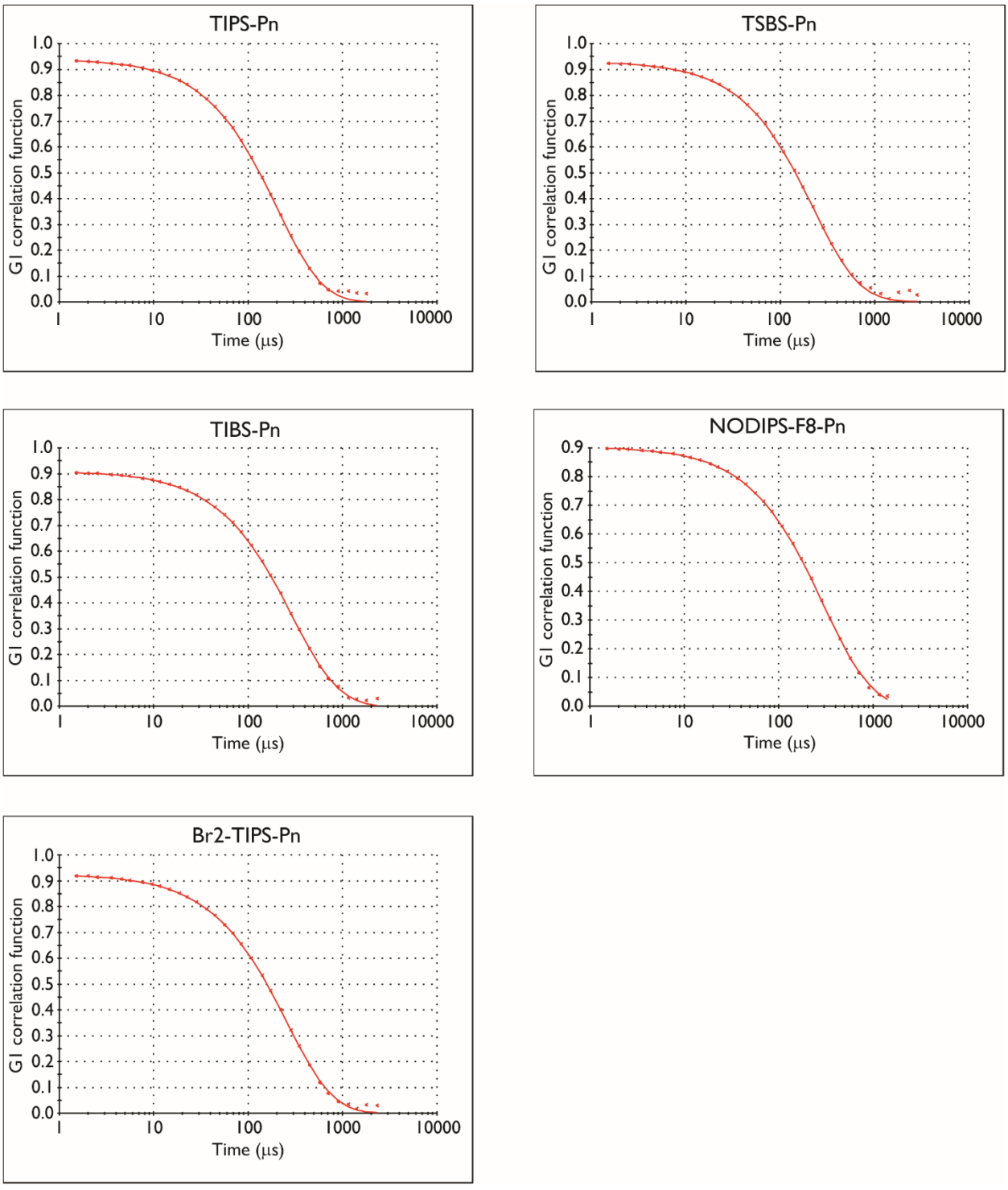

Figure S3. Autocorrelation functions from dynamic light scattering measurements of aqueous colloidal TSBS-, TIPS-, TIBS-, F8-NODIPS -, and Br2-TIPS-pentacene nanoparticles obtained at 25 °C.

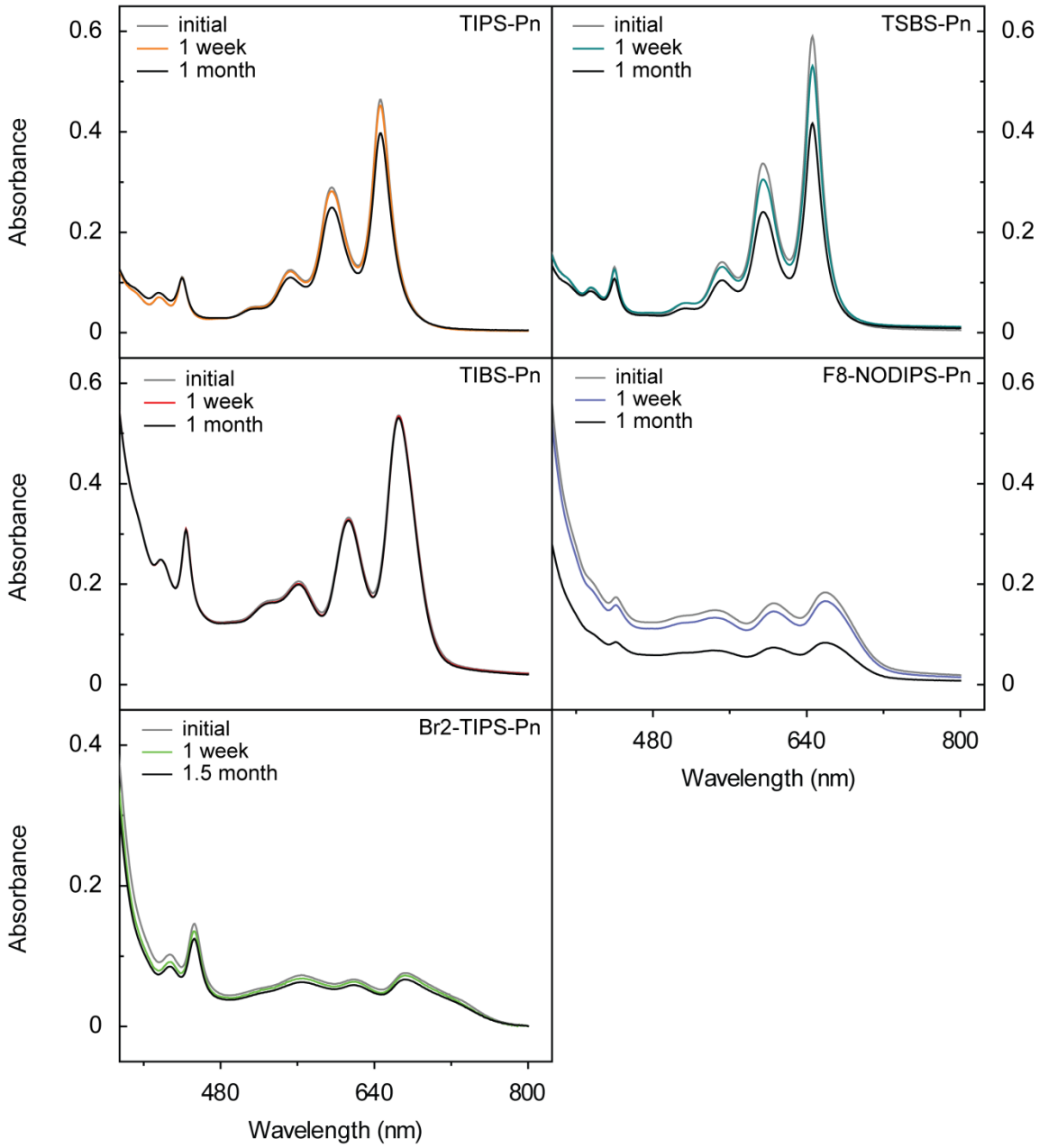

Figure S4. Electronic absorption spectra of aqueous colloidal TIPS-, TSBS-, TIBS-, F8-NODIPS-, and Br2-TIPS-pentacene nanoparticles measured one week and one month after their preparation. These data have not been baseline subtracted or normalized. The samples were stored in the dark for the duration of these measurements. All of the nanoparticles with the exception of the TIBS-Pn nanoparticles precipitated out of solution as a fine black solid which

was manifest as a decreasing signal amplitude with storage time. The nanoparticles did not exhibit signs of significant chemical decomposition during this period of time.

Solvatochromic study of ^1L_a transition of TIPS-Pn

To clarify the origin of the redshift of the lowest-energy singlet transition in the TIPS-Pn nanoparticles, we measured the absorption and fluorescence spectra of TIPS-Pn dissolved in various solvents. We found that the ^1L_a transition redshifts when going from nonpolar solvents such as *n*-hexane to more polarizable, aromatic solvents such as chloroform and toluene (Figure S5 and Table S1). From these data, it is apparent that the absorption spectrum of TIPS-Pn in toluene most closely resembles that of the chromophore in the nanoparticle. These results suggest that the solvent environment representative of the bulk of the nanoparticle is most similar to toluene, as might be anticipated by the similarity of toluene and the Pn core. Critically, these data also confirm that the changes observed in the nanoparticle absorption spectra are not a result of the influence of the surrounding aqueous environment. While we were unable to measure the absorption spectrum of TIPS-Pn in water (TIPS-Pn is insoluble in water), this conclusion is based on the observation that the ^1L_a transition of TIPS-Pn is *blue-shifted* in polar protic solvents such as methanol, ethanol, and 2-propanol. We note that the linewidth of the lowest-energy singlet transition in the nanoparticles is also slightly broader than the linewidth of the corresponding feature of TIPS-Pn in any solvent (Table S1). The broader linewidth observed in the absorption spectrum of the nanoparticles could have several possible origins including differences in the distribution of environments in which the chromophores exist (i.e. inhomogeneous broadening), differences in homogeneous broadening, or splitting of the lowest-energy singlet transition (i.e. excitonic effects).

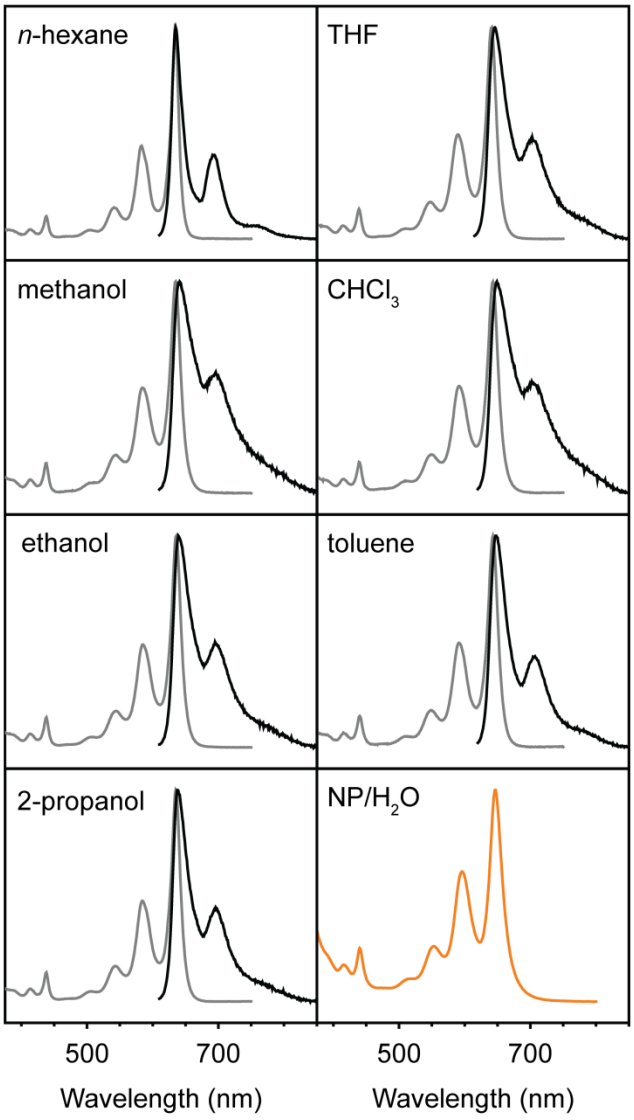

Figure S5. Solvatochromism of the ^1L_a transition of TIPS-pentacene: steady-state absorption and fluorescence spectra. Steady-state absorption (blue) and fluorescence (grey) spectra of a solution of TIPS-Pn in *n*-hexane, methanol, ethanol, 2-propanol, tetrahydrofuran, chloroform, and toluene and absorption spectrum of an aqueous colloidal suspension of TIPS-pentacene nanoparticles (orange). All data plotted have been normalized. The solutions were not degassed prior to the measurement. The TIPS-pentacene nanoparticles lack any readily observable fluorescence.

Solvent	$\lambda_{abs,max}$ (nm)	$FWHM_{abs,0\text{-}0}$ (cm^{-1})	$A_{0\text{-}0}/A_{0\text{-}1}$	$\lambda_{em,max}$ (nm)	$FWHM_{em,0\text{-}0}$ (cm^{-1})	Δ_{Stokes} (cm^{-1})
n-hexane	634	340	2.3	635	490	25
methanol	635	480	2.0	641	1110	150
ethanol	636	430	2.1	639	840	70
2-propanol	635	410	2.1	638	710	70
acetone	638	520	1.9	647		210
tetrahydrofuran	641	450	2.0	646	840	120
chloroform	643	480	2.0	649	1050	140
toluene	643	460	2.0	647	730	100
NP/water	646	550	1.6			

Table S1. Observables Obtained from Steady-State Absorption and Fluorescence Spectra of TIPS-pentacene Dissolved in Various Solvents. The peak of the absorption and fluorescence spectra in the vicinity of the ^1L_a transition of TIPS-Pn was obtained by determining the maximum value in the raw data (i.e. the values were not obtained by fitting the data). The FWHM represents the full-width at half maximum of the 0–0 vibronic transition appearing in the absorption and fluorescence spectra. $A_{0\text{–}0}/A_{0\text{–}1}$ represents the ratio of the amplitudes of the 0–0 and 0–1 vibronic peaks in the absorption spectrum. The Stokes shift was taken as the energy difference between the peak of the 0–0 absorption and 0–0 fluorescence spectral features. The linewidths were too broad to allow for an accurate measure of the FWHM of the lineshapes appearing in the fluorescence spectrum of TIPS-Pn in acetone. The ^1L_a transition of TIPS-Pn redshifts on going from nonpolar solvents (such as *n*-hexane) and polar protic solvents (such as methanol and ethanol) to more polarizable, aromatic solvents (such as chloroform and toluene) whose spectra more closely resemble that of the aqueous colloidal TIPS-Pn nanoparticles.

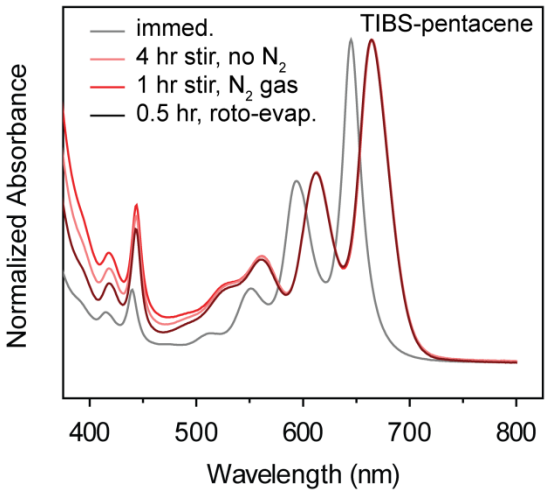

Figure S6. Electronic absorption spectra of aqueous colloidal TIBS-pentacene nanoparticles immediately after injection and following various means of driving off the residual THF. These measurements were made when the mass of the solution was either the same or less than prior to injection (i.e. most of the residual THF had been driven off), with the exception of the spectrum denoted "immed." which was measured immediately following injection of the TIBS-Pn/THF solution into the water. The spectrum denoted "4 hr stir, no N_2 gas" was measured after letting the solution stir for about 4 hours prior to measuring the spectrum. The spectrum denoted "1 hr stir, N_2 gas" was measured with nitrogen gas bubbling through the solution and letting the solution stir for about 1 hour before measuring the spectrum. The spectrum denoted "roto-evap." was measured after subjecting the solution to rotary evaporation at ~75 torr and ~40 ^{o}C for ~30 minutes before measuring the spectrum. All data have been normalized to the peak of the 0–0 band of the lowest-energy singlet transition.

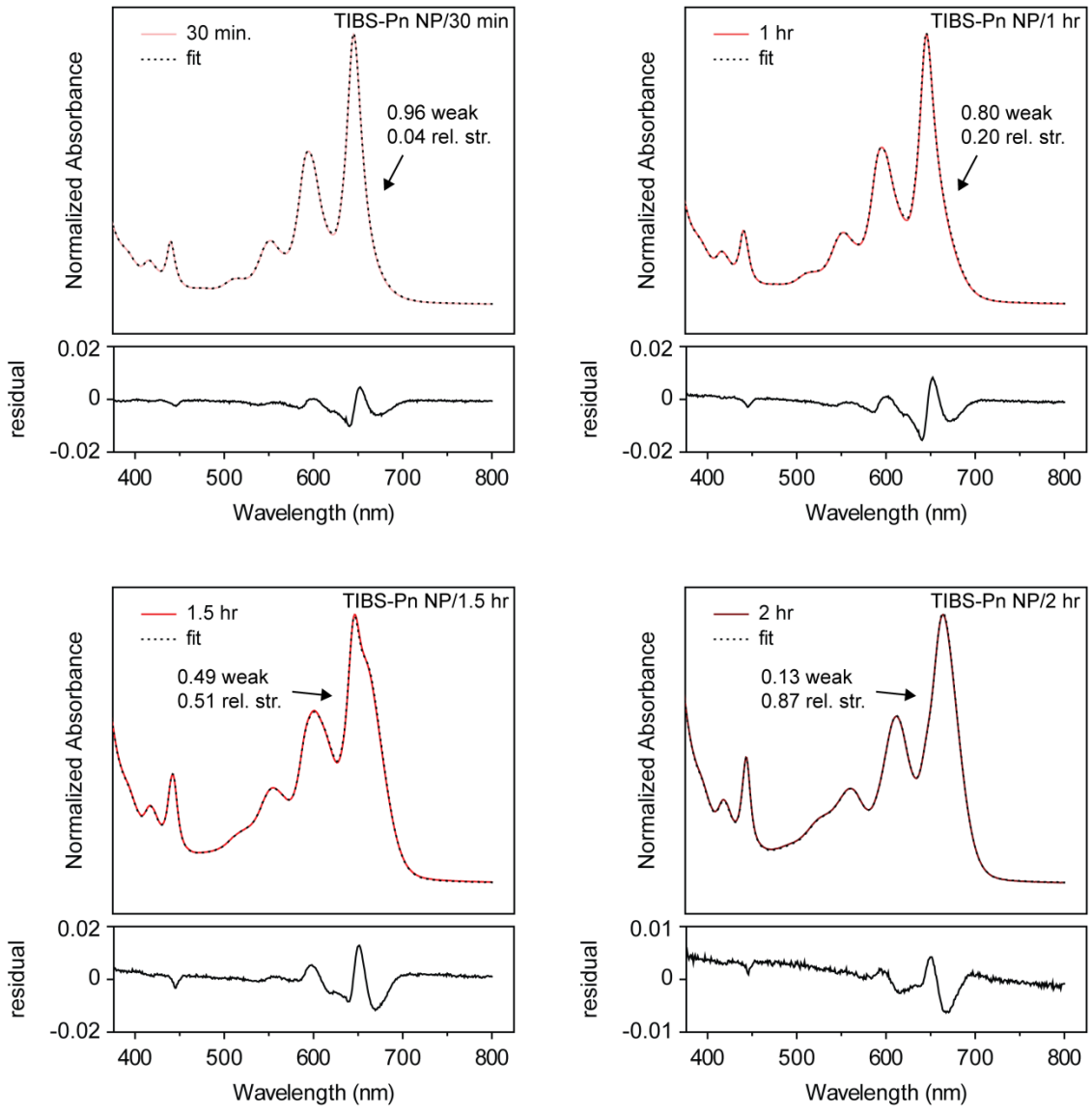

Figure S7. Electronic absorption spectra of aqueous colloidal TIBS-pentacene nanoparticles, including fits and corresponding residual, as a function of time following TIBS-pentacene/THF solution injection (with the residual THF driven off in air). We fit the intermediate time spectra with a linear combination of the initial and final spectra. We are able to accurately model the data and quantify the relative populations of weakly coupled and more strongly coupled chromophores in the TIBS-Pn nanoparticles. Quantification in this manner is

limited by the assumption that the initial and final populations are predominantly weakly and more strongly coupled chromophores, respectively. With this assumption in mind, the relative contribution of initial (weakly coupled chromophore) and final (more strongly coupled chromophore) spectra to the intermediate time spectrum is indicated in each panel.

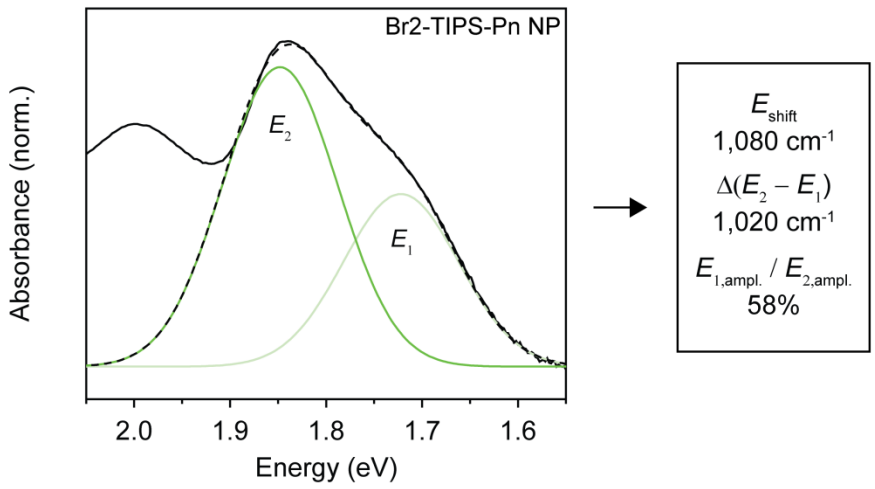

Figure S8. Electronic absorption spectra of aqueous colloidal Br2-TIPS-Pn nanoparticles and Gaussian fits to the split 0–0 band of the lowest-energy singlet transition. A Jacobian conversion of the data (obtained as a function of wavelength) was carried out in order to perform a quantitative analysis in the energy domain.[S2] A sum of two Gaussians was used to model the 0–0 band of the TIPS-Br2-Pn nanoparticle absorption spectrum. The exciton shift and splitting for the Br2-TIPS-Pn chromophores according to this simple model were ~1,080 and ~1,020 cm^{-1}, respectively. The exciton shift was taken as the difference between the mean of the transition energies of the two Gaussian features and the ^1L_a transition energy of Br2-TIPS-Pn dissolved in toluene. The ratio of E_1/E_2 Gaussian peak amplitudes was ~58%.

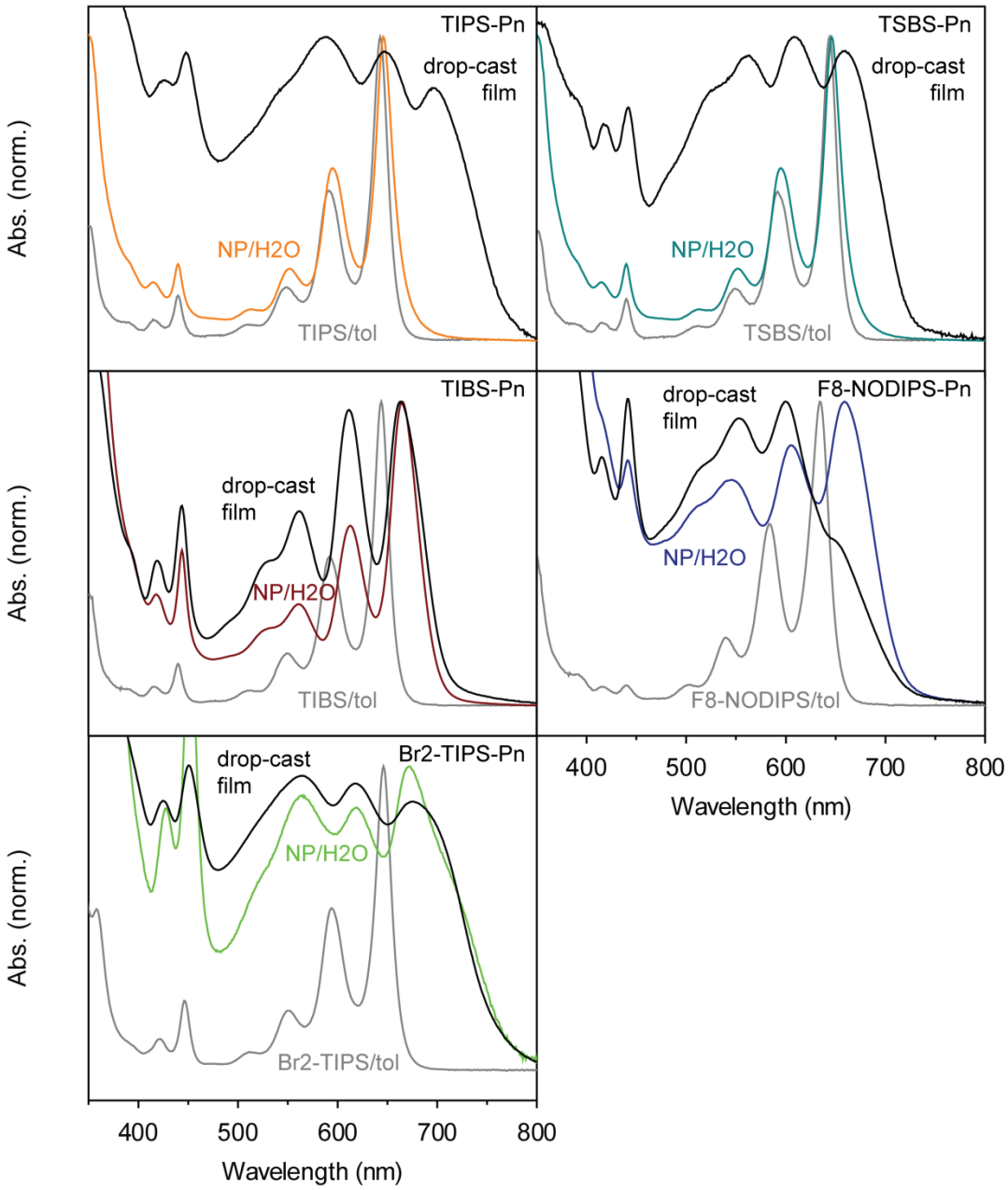

Figure S9. Electronic absorption spectra of TIPS-, TSBS-, TIBS-, F8-NODIPS-, and Br2-TIPS-Pn dissolved in toluene as well as the respective aqueous colloidal nanoparticles and drop-cast films. The data were normalized to the most intense spectral feature in the vicinity of the lowest-energy singlet transition. The absorption spectra of the TIPS- and TSBS-Pn nanoparticles are more comparable to the absorption spectra of the respective compound

dissolved in toluene whereas the absorption spectra of TIBS-, F8-NODIPS-, and Br2-TIPS-Pn nanoparticles are more comparable to the absorption spectra of drop-cast films of the respective compound.

	Φ_F	
Pn Derivative	THF	NP/H_2O
TIPS	0.32	~0.9×10^{-4}
TSBS	0.36	~1×10^{-4}
TIBS	0.36	< 1×10^{-4}
F8-NODIPS	0.28	< 1×10^{-4}
Br2-TIPS	0.24	< 1×10^{-4}

Table S2. Relative Fluorescence Quantum Yield of TIPS-, TSBS-, TIBS-, F8-NODIPS- and Br2-TIPS-pentacene Dissolved in THF and of the Corresponding Aqueous Colloidal Nanoparticle Suspensions. Oxazine-1 in ethanol (Φ_F=0.14)[S3] was used as a relative fluorescence quantum yield standard. The solutions were de-oxygenated by bubbling nitrogen gas through the solution for at least 15 minutes immediately prior to the measurements.

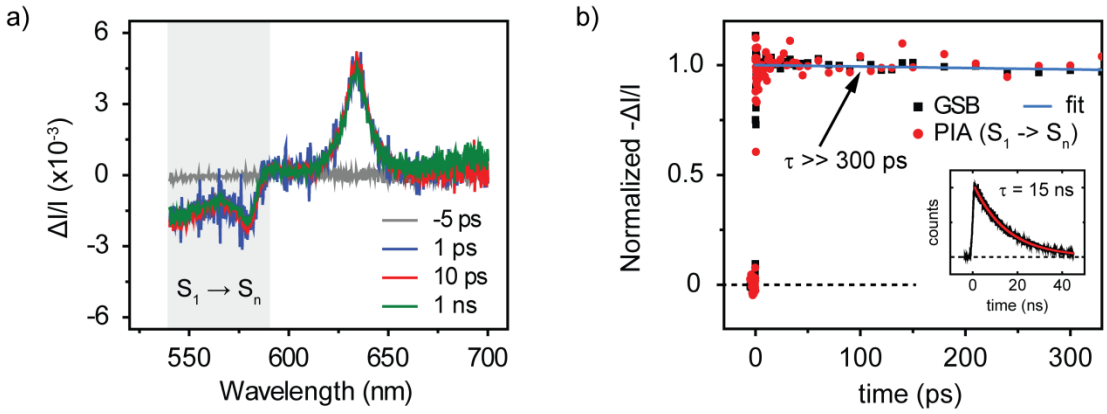

Figure S10. Pump–probe measurements on TIPS-pentacene dissolved in *n*-hexane. (a) Transient absorption spectra of TIPS-Pn dissolved in *n*-hexane at pump–probe time delays of -5, 1, 10, and 1000 ps. (b) Transient kinetics of the ground-state bleach (GSB) and singlet photoinduced absorption (PIA). The ground-state bleach signal was taken as the mean over the spectral range 625 to 640 nm. The region where the singlet photoinduced absorption is most apparent is highlighted in grey in panel a. The singlet photoinduced absorption signal was taken as the mean over the spectral range 555 to 580 nm. The optical density of the sample at the maximum of the ^1L_a transition was ~0.05. The pump–probe measurements were performed with an incident pump fluence of ~400 μJ/cm^2 (corresponding to an absorbed fluence of ~20 μJ/cm^2). The inset in panel b includes a TCSPC measurement of TIPS-pentacene in *n*-hexane. Overlaying these data is a single exponential fit corresponding to a ~15 ns time constant.

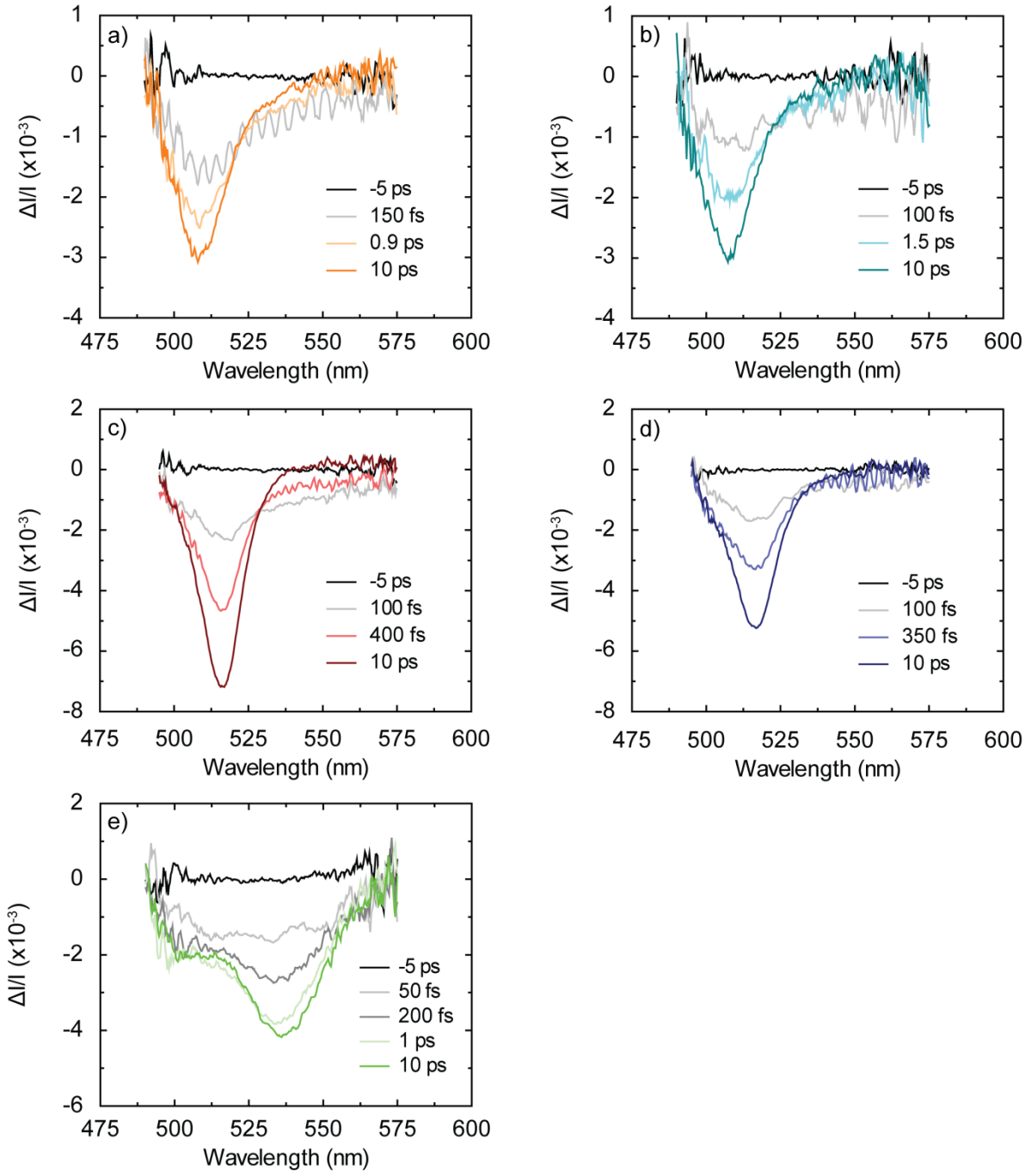

Figure S11. Transient absorption spectra of aqueous colloidal TIPS-, TSBS-, TIBS-, F8-NODIPS-, and Br2-TIPS-pentacene nanoparticles in the spectral range between ~490 and 575 nm covering both singlet and triplet photoinduced absorptions. a-e, Transient absorption spectra of (a) TIPS-, (b) TSBS-, (c) TIBS-, (d) F8-NODIPS-, and (e) Br2-TIPS-pentacene

nanoparticles. These experiments were carried out on samples with an optical density of ~0.06 or less in the vicinity of the NOPA spectrum and with an incident pump fluence less than or equal to ~30 $\mu J/cm^2$ (corresponding to an absorbed pump fluence of ~4 $\mu J/cm^2$ or less).

Average number of excitons and exciton mean distance

We estimated the average number of excitons per nanoparticle by taking the product of the pump photon fluence and particle cross section.[S9,S10]

The incident pump fluence was estimated as reported in the main text. The pump photon fluence was obtained by normalizing the laser pulse spectrum such that the area was unity; the product of the incident pump fluence (in units of $\mu J/cm^2$) with the laser pulse spectrum normalized in this manner divided by the energy per photon at each wavelength gave the pump photon fluence.

The particle cross section was estimated as the product of the cross section of the molecules in the nanoparticle with the number of molecules comprising the nanoparticle. The cross section of the molecules in the nanoparticles was estimated from measurements on the molecular cross section of the chromophores in dilute solution, measurements on the molecular cross section of the chromophores embedded in the nanoparticles, and from the different attenuation of the molecular cross section in the nanoparticles of the various compounds as discussed in the main text (see, specifically, Fig. 8). Taking the nanoparticle diameter from the dynamic light scattering measurements, along with the density (as approximated by that of TIPS-Pn),[S11] the molecular weight, and Avogadro's number, gave the number of molecules per nanoparticle. This was of the order of several hundred thousand molecules for the ca. 100 nm diameter nanoparticles (Table S3). The particle cross section was of the order of ca. 1×10^{-11} cm^{-2} in all cases (Table S3).

We estimated the mean distance between excitons by taking the third root of the inverse of the exciton density in the nanoparticles. This estimation assumes a homogeneous spatial

distribution of excitons. The exciton density in the nanoparticles was taken as the average number of excitons per nanoparticle divided by the nanoparticle volume.

According to these calculations and at the incident pump photon fluences of these measurements, the average number of excitons per nanoparticle ranged from ca. 100-700 excitons/nanoparticle for the ca. 100 nm diameter nanoparticles and the mean distance between excitons ranged from ca. 8-12 nm/exciton (Table S3). The mean distance between excitons is in the regime of the typical singlet exciton diffusion length of ~10 nm reported for solid-state media of organic chromophores[S12,S13] suggesting that singlet-singlet annihilation should be insignificant at these pump photon fluences. This assertion is consistent with the fluence-dependent measurements reported and discussed in the main text (see for example Fig. 6).

Pn Derivative	Average Number Excitons / Exciton Mean Distance							
	$j_{pu,incident}$ ($\mu J/cm^2$)	$j_{pu,incident}$ (ph/cm^2)	ϕ_{NP} (nm)	N_{molec}	0–0 band peak $\varepsilon_{molec,NP}$ ($M^{-1}\,cm^{-1}$)	0–0 band peak $\sigma_{NP,\,H2O}$ (cm^{-2})	$<N_{ex}>$	d_{ex} (nm)
TIPS	30	8×10^{13}	69	1.8×10^{5}	2.0×10^{4}	1.4×10^{-11}	150	11
TSBS	30	8×10^{13}	76	2.1×10^{5}	2.0×10^{4}	1.6×10^{-11}	140	12
TIBS	30	8×10^{13}	94	4.0×10^{5}	1.5×10^{4}	2.1×10^{-11}	350	11
F8-NODIPS	30	8×10^{13}	98	3.5×10^{5}	1.0×10^{4}	1.4×10^{-11}	730	9
Br2-TIPS	50	1×10^{14}	81	2.3×10^{5}	8.0×10^{3}	1.1×10^{-11}	670	8

Table S3. Experimental Measurements and Parameters Used to Estimate the Average Number of Excitons and Exciton Mean Distance.

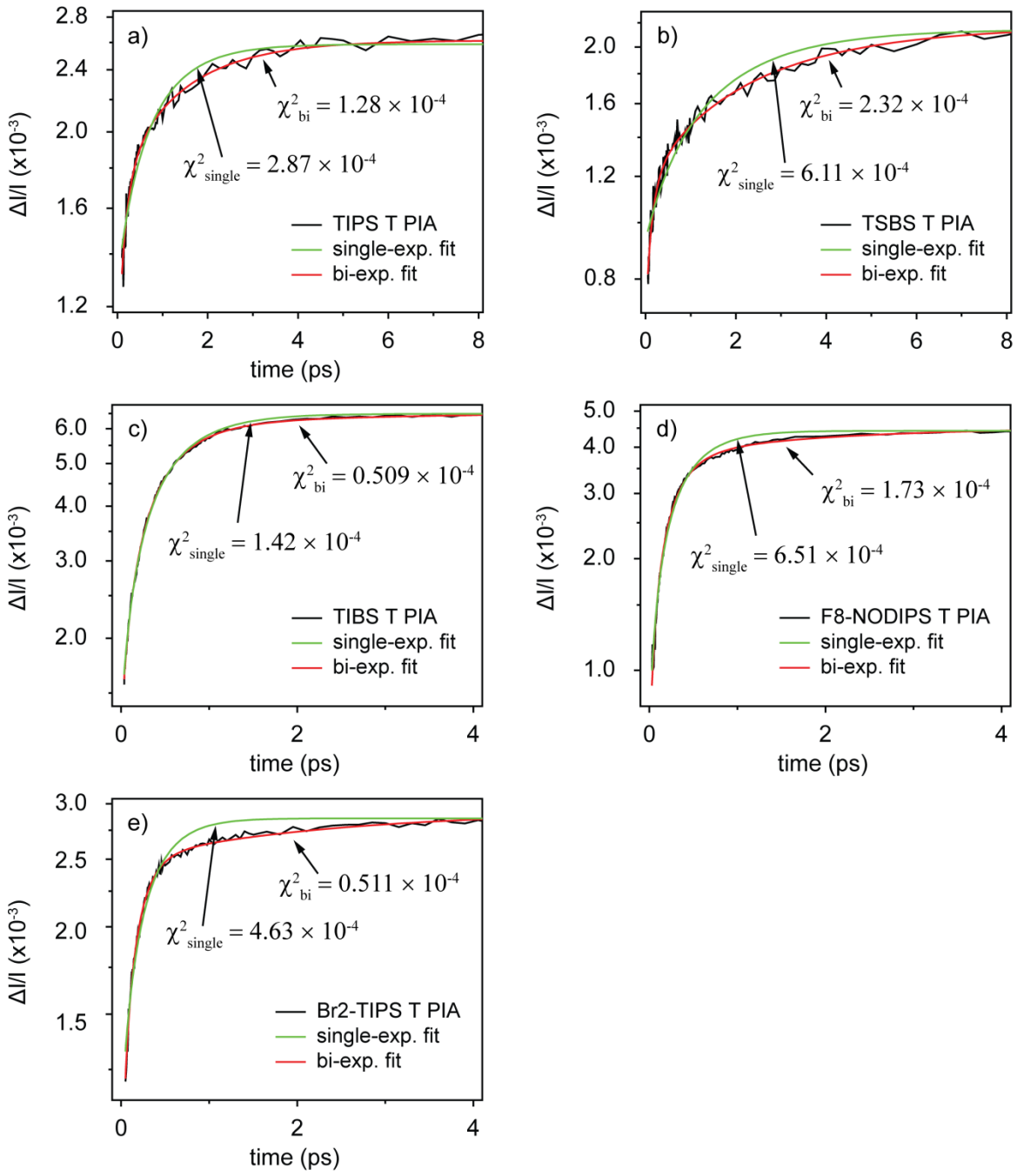

Figure S12. Semilog plots comparing single- and bi-exponential fits to amplitude of triplet photoinduced absorption signal appearing in TIPS-, TSBS-, TIBS-, F8-NODIPS-, and Br2-TIPS-pentacene nanoparticle transient absorption spectra as a function of pump−probe time delay. (a) TIPS-, (b) TSBS-, (c) TIBS-, (d) F8-NODIPS-, and (e) Br2-TIPS-Pn nanoparticle

triplet PIA signal amplitude as a function of pump–probe time delay and associated single- and bi-exponential fits. The value of Pearson's χ^2 obtained from this analysis for each fit is reported in the figure. A bi-exponential function consistently provides a better representation of these data. The ratio of the χ^2 value obtained from the single- and bi-exponential fits is greater than 220% in all cases.

Nonexponential singlet fission kinetics

Johnson and co-workers have previously highlighted that nonexponential kinetics are often observed in polycrystalline films of singlet fission chromophores.[S14]

Singlet fission through high-lying excited states could give rise to nonexponential triplet formation kinetics. Schrauben *et al.*, for example, recently reported bi-exponential kinetics in polycrystalline films of 1,3-diphenylisobenzofuran at high pump fluence that converged to single-exponential kinetics at low pump fluence.[S15] The interested reader can find a detailed kinetic scheme in Schrauben *et al.* along with associated discussion. A fast time constant of ~200 fs, only observed at high fluence, was attributed to singlet fission through high-lying singlet excited states accessed via multiphoton absorption that occurred in competition with vibrational relaxation. At low fluence the intrinsic timescale of singlet fission was recovered in the form of a single exponential with a time constant of ~30 ps. Thermally activated singlet fission (i.e. singlet fission through high-lying vibrational quanta of the lowest-excited singlet state) could also give rise to nonexponential triplet formation kinetics, but is not considered in the present work as singlet fission is anticipated to be exoergic for the Pn derivatives studied here.

Nonexponential triplet formation kinetics could also be observed when singlet fission occurs in solids containing molecular packing arrangements exhibiting varying degrees of electronic coupling. For example,

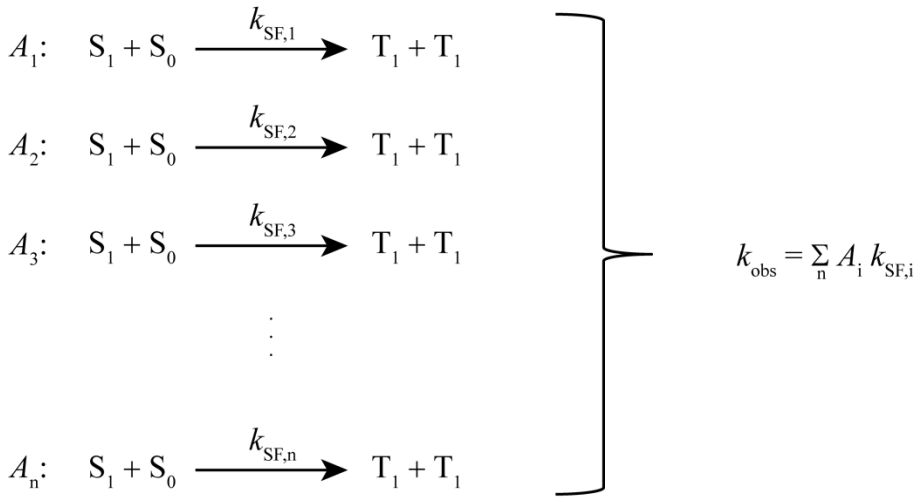

where, for the sake of simplicity, we have omitted the correlated triplet pair and assumed that the singlet fission process is unidirectional. We note that contemporary theories of singlet fission[S16,S17] predict that the rate would be affected by both electronic coupling as well as energy level matching.[S18,S19] The clearest example of the occurrence of different singlet fission rates as a function of molecular packing arrangement is manifest in studies on different crystal polymorphs. Dillon *et al.*, for example, observed different rates of triplet pair formation, i.e. k_{-2}, in monoclinic and orthorhombic forms of 1,6-diphenyl-1,3,5-hexatriene.[S20] The rate of triplet pair formation differed by almost a factor of 2 in the different crystal polymorphs. More recently, various Pn derivatives have been utilized to elucidate differences in singlet fission dynamics as a function of molecular packing arrangement. Herz *et al.*, for example, suggested that the factor of two faster singlet fission rate observed in a film of a diaza-TIPS-Pn derivative (compared with a film of TIPS-Pn) may be a result of tighter packing and stronger electronic coupling.[S21] In corroboration with this report, Wu *et al.* reported a factor of two faster time constant for triplet formation via singlet fission in a film of an anthradipyridine-modified Pn derivative that exhibited a slightly smaller intermolecular distance relative to TIPS-Pn (a difference of ~0.1 Å).[S22] These authors also reported that the film of the anthradipyridine-modified Pn derivative

exhibited a greater overall triplet yield, although the triplet yield observed in the TIPS-Pn film differed from a previous report by Ramanan *et al*.[S23]

Lastly, multiple phases of triplet formation including energy-migration limited singlet fission could be a possible origin of nonexponential triplet formation kinetics. Roberts *et al.* developed a kinetic model to account for multiple phases of triplet formation in disordered systems by incorporating a component associated with exciton diffusion to sites with molecular packing arrangements suitable for singlet fission, i.e. energy-migration limited singlet fission.[S19] The interested reader is referred to section VII of that work for a detailed discussion and illustration of the kinetic model. In transient absorption experiments on disordered films of 5,12-diphenyltetracene, Roberts *et al.* clearly observed the simultaneous nonexponential decay and growth of singlet and triplet populations. The model developed by Roberts *et al.* assumed that in disordered molecular solids a subset of molecular pairs adopt a packing arrangement suitable for singlet fission. An exciton not in the immediate vicinity of molecules with the proper packing arrangement for singlet fission must diffuse to those sites where singlet fission can occur. Roberts *et al.* considered triplets being generated over the course of two timescales in their model. The faster phase of triplet formation was attributed to the intrinsic timescale of singlet fission, while the latter, slower triplet formation phase was attributed to energy-migration limited singlet fission.

Extent of solid-state order in nanoparticles of pentacene derivatives

Additional pump–probe anisotropy measurements enable clarification of the extent of solid-state order in the nanoparticles. We first measured the anisotropy decay of the ground-state bleach of TIBS-Pn dissolved in THF. We found that the anisotropy value is initially near the theoretical maximum of 0.4 and decays to a value of 0 with a time constant of ~150 ps (Figure S13). These observations are consistent with re-orientational dynamics frequently observed of chromophores in dilute solution.[S24]

To clarify the extent of solid-state order in the nanoparticles, we first measured the anisotropy decay in the limit of one extreme, i.e. energy migration in a medium anticipated to exhibit extensive long-range solid-state order, by measuring the ground-state bleach anisotropy decay in the TIBS-Pn nanoparticles (Figure S14). In the case of an ordered assembly of molecules, an energy transfer event would not be anticipated to significantly re-orient the chromophore's transition dipole. We find that, consistent with our expectation for an ordered assembly of molecules comprising the TIBS-Pn nanoparticles, the anisotropy of the ground-state bleach does not decay appreciably on the picosecond timescale. Indeed, the anisotropy value averaged over the time range ~100 to 400 fs is ~0.38, indicating that the initially photo-excited exciton does not re-orient significantly on a timescale where energy transfer may occur (i.e. immediately preceding singlet fission). For comparison with the opposite extreme, i.e. energy migration in a medium expected to have very little long-range solid-state order, we measured the anisotropy decay of TIBS-Pn nanoparticles where a significant fraction of the initial injection solvent, THF, remained present in the aqueous colloidal suspension. As demonstrated in Figs. 2 and 3 of the main text, the presence of THF in the aqueous colloidal nanoparticle suspension inhibits packing motifs that promote stronger electronic interactions in the TIBS-, F8-NODIPS-,

and Br2-TIPS-Pn nanoparticles; thus, the presence of THF inhibits long-range solid-state order. We find that the depolarization of the ground-state bleach feature of the TIBS-Pn nanoparticles in the presence of THF is nearly equivalent to that of the TIPS- and TSBS-Pn nanoparticles, indicating that the TIPS- and TSBS-Pn nanoparticles indeed have very little long-range solid-state order. Taken together, these data indicate that, as an aqueous colloidal suspension in solution, the TIPS- and TSBS-Pn nanoparticles (Type I) have little long-range order, whereas the TIBS-Pn nanoparticles (Type II) exhibit extensive long-range solid-state order.

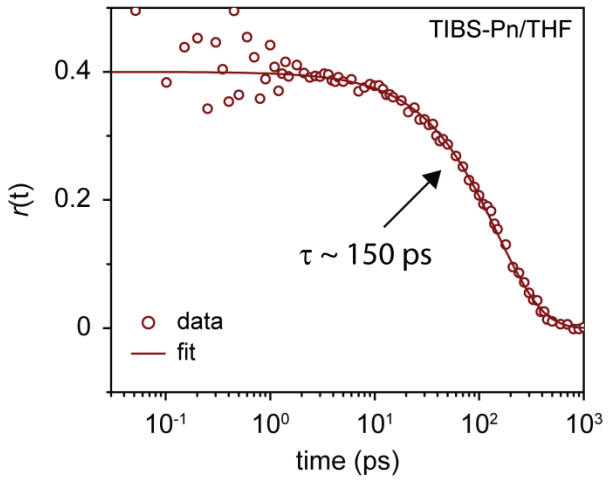

Figure S13. Pump–probe anisotropy of the 0–0 ground-state bleach feature of TIBS-Pn dissolved in THF. The anisotropy decay of the 0–0 ground-state bleach feature appearing in the transient spectra of TIBS-Pn dissolved in THF was taken as the mean over the spectral range 634 to 652 nm. The anisotropy value is initially near the theoretical maximum of 0.4 and decays to a value of 0 with a time constant of ~150 ps. These results are consistent with re-orientational dynamics frequently observed of chromophores in dilute solution. This experiment was carried out on a sample with an optical density of ~0.24 or less in the vicinity of the NOPA spectrum and with an incident pump fluence of ~90 μJ/cm^2.

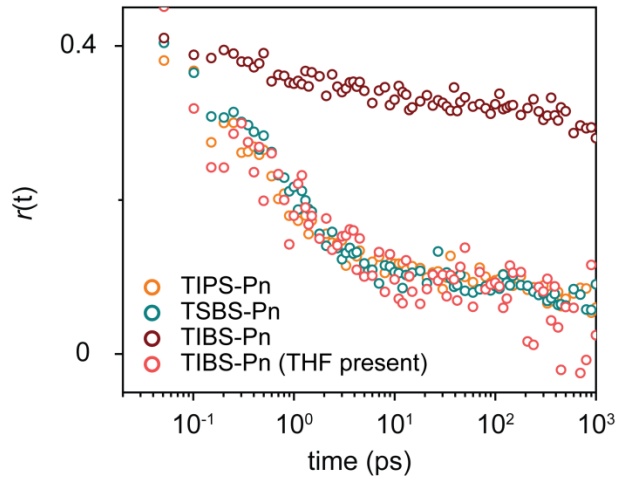

Figure S14. Pump–probe anisotropy of the 0–0 ground-state bleach feature of TIPS-, TSBS-, and TIBS-pentacene nanoparticles in the absence of THF as well as TIBS-pentacene nanoparticles in the presence of THF. The anisotropy decay of the 0–0 ground-state bleach appearing in the transient spectra of the TIPS- and TSBS-pentacene nanoparticles (in the absence of THF) and TIBS-pentacene nanoparticles (in the presence of THF) was taken as the mean over the spectral range 640 to 660 nm. The corresponding decay for the TIBS-pentacene nanoparticles (in the absence of THF) was taken as the mean over the spectral range 655 to 685 nm. The anisotropy decays of the TIPS- and TSBS-pentacene nanoparticles (in the absence of THF) and TIBS-pentacene nanoparticles (in the presence of THF) are similar, each exhibiting a rapid depolarization reaching a non-zero offset on the picosecond timescale. The anisotropy of the TIBS-pentacene nanoparticles (in the absence of THF), in contrast, does not decay appreciably prior to or following singlet fission. These data strongly support the interpretation that the TIPS- and TSBS-pentacene nanoparticles in solution have little long-range order whereas the TIBS-pentacene nanoparticles exhibit extensive long-range solid-state order. These

experiments were carried out on samples with an optical density of ~0.20 or less in the vicinity of the NOPA spectrum and with an incident pump fluence of ~90 $\mu J/cm^2$.

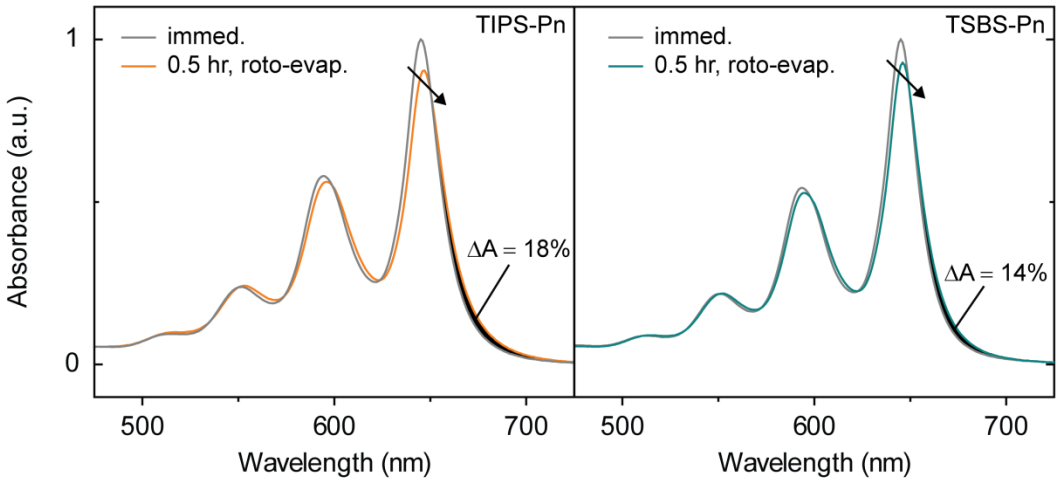

Figure S15. Electronic absorption spectra of aqueous colloidal TIPS- and TSBS-pentacene nanoparticles as a function of time following injection of the pentacene derivative/THF solution. The absorption spectra of the nanoparticles measured immediately following injection of the Pn derivative/THF solution was normalized to the maximum intensity of the lowest-energy singlet transition; the absorption spectra of the nanoparticles measured after driving off the residual THF from the solution was scaled by the same factor used to normalize the previous data. Similar to the TIBS-Pn nanoparticles, we observe what would appear to represent isosbestic points in the vibronic bands indicating the interconversion between two populations, a population of weakly coupled chromophores and a population of lower energy, more strongly coupled chromophores. The fractional change in population was assayed by integrating the area in the region beyond the proposed isosbestic point of the 0–0 vibronic band of the spectra, taking the ratio, and taking the difference with unity (i.e. ΔA). The TIPS-Pn nanoparticles appear to exhibit a slightly larger population of more strongly coupled chromophores relative to the TSBS-Pn nanoparticles.

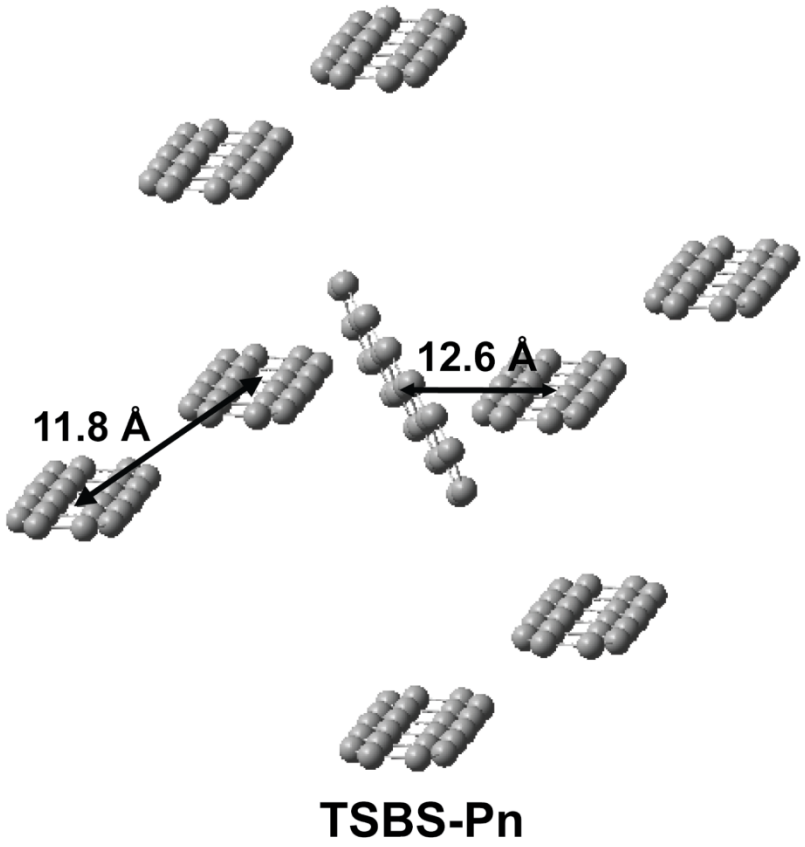

Figure S16. Solid-state order of TSBS-pentacene. These data were obtained from the single crystal X-ray data. Hydrogen atoms and side chains have been omitted for clarity. The arrows superimposed on the data represent the center-to-center distance between molecules measured relative to the center of the pentacene core. Note the seeming absence of π-stacking. We highlight and note also that the solid-state order depicted here represents a linear combination of the mixture of diastereomers comprising the bulk crystal.

Pentacene derivative nanoparticle powder X-ray diffraction experiments

To better understand the relative crystallinity of the nanoparticles we measured X-ray diffractograms of nanoparticle powders prepared by concentrating the aqueous colloidal nanoparticle suspensions and subsequently completely dehydrating the suspension through freeze drying. X-ray diffractograms of powders of the Type II nanoparticles feature multiple intense Bragg reflections indicating that the nanoparticle powders are crystalline (Figure S17). The most intense reflections occur at 7.26, 4.04, and 4.89° in the nanoparticle powders of TIBS-, F8-NODIPS-, and Br2-TIPS-Pn, respectively, and correspond to d-spacings of 12.2, 21.9, and 18.1 Å that are generally consistent with the interlayer spacing in the respective single crystals. The interpretation that the d-spacing corresponds to the interlayer spacing is supported by the large d-spacing observed for F8-NODIPS-Pn, which is expected due to the relatively long *n*-octyl chains of the peripheral silyl groups.

To further aid in interpreting the X-ray diffractograms of Type II nanoparticles, we compared them with X-ray diffractograms predicted from the single crystal and of polycrystalline powders. TIBS-Pn agrees very well with the powder diffractogram of the polycrystalline powder (Figure S17), and thus we conclude that the molecular packing arrangement in TIBS-Pn nanoparticles must strongly resemble that of a typical polycrystalline film. Bragg reflections in the range $2\theta = 10–30°$ of the TIBS-Pn nanoparticle powder diffractogram appear in the diffractogram predicted from the single crystal, while some predicted from the single crystal are absent. Nevertheless, the very close similarity between the nanoparticle diffractogram and that of the crystalline powder strongly suggests that TIBS-Pn nanoparticles are crystalline. In the case of F8-NODIPS-Pn, good agreement between the two experimentally obtained diffractograms and that predicted from the single crystal is observed,

suggesting correspondence to the bulk structure. The diffractogram of the Br2-TIPS-Pn nanoparticle powder shows peaks overlapping those predicted from the single crystal and in the crystalline powder, indicating that domains of the bulk crystalline form are present in the nanoparticle powder. Peaks in the nanoparticle powder diffractogram of Br2-TIPS-Pn not predicted from the single crystal or present in the crystalline powder are also apparent, indicating the presence of domains with other molecular packing arrangements, possibly due to isomers present in the sample.

The X-ray diffractograms of powders of TIPS-Pn and TSBS-Pn nanoparticles display several Bragg reflections indicating they are also crystalline (Figure S18). Given the substantial evidence already presented that the Type I nanoparticles in their native state (i.e. as aqueous colloidal suspensions) lack long-range solid-state order, we suggest that the powder preparation conditions induce this crystallinity. This is particularly evident for nanoparticles of TIPS-Pn where the experimentally obtained powder X-ray diffractogram quite closely matches the one predicted from the single-crystal structure. As such, the absorption spectrum of the TIPS-Pn nanoparticles measured in solution should exhibit the corresponding absorption features of the crystalline form (which it does not).

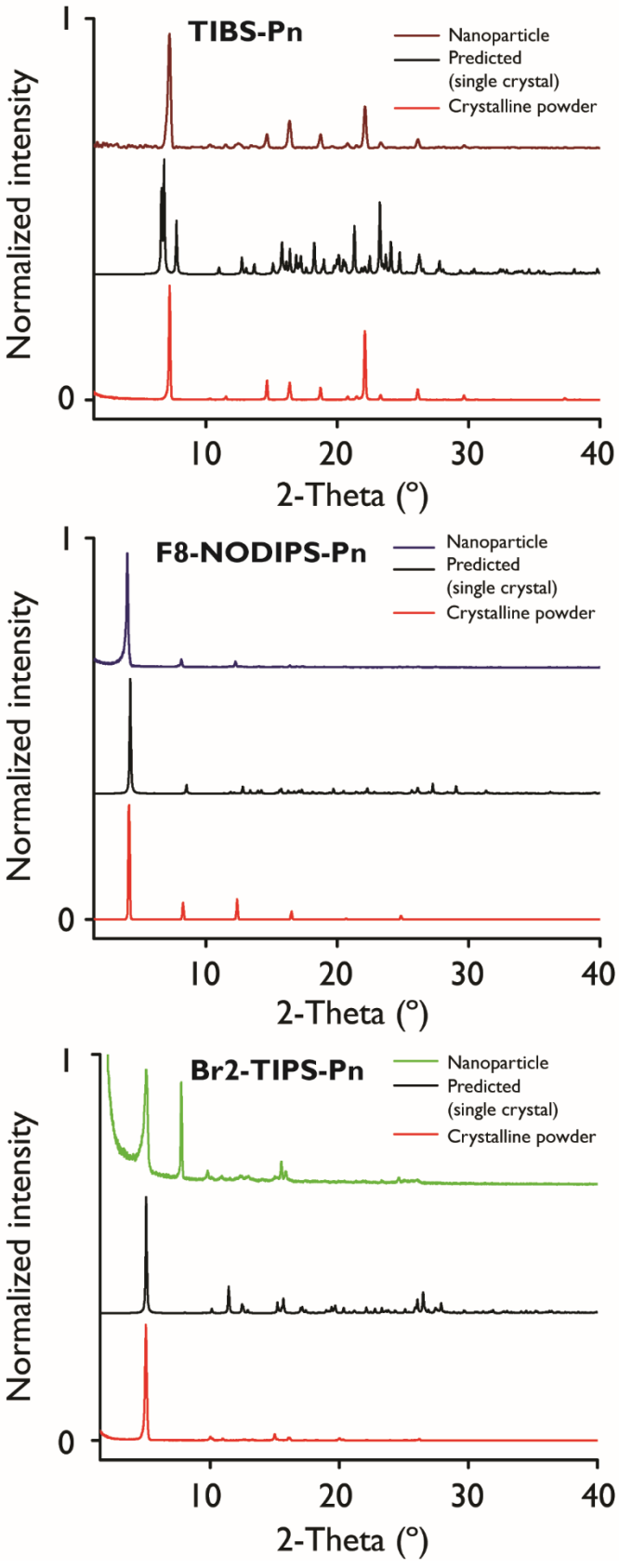
TIBS-Pn
Nanoparticle
Predicted
(single crystal)
Crystalline powder
Normalized intensity
1
0
10
20
30
40
2-Theta (°)
F8-NODIPS-Pn
Nanoparticle
Predicted
(single crystal)
Crystalline powder
Normalized intensity
1
0
10
20
30
40
2-Theta (°)
Br2-TIPS-Pn
Nanoparticle
Predicted
(single crystal)
Crystalline powder
Normalized intensity
1
0
10
20
30
40
2-Theta (°)

Figure S17. Nanoparticle, predicted (single crystal), and crystalline powder X-ray diffractograms of TIBS-, F8-NODIPS-, and Br2-TIPS-pentacene. The nanoparticle powder X-ray diffractograms are qualitatively comparable to the powder X-ray diffractograms of the crystalline powder in all cases. In the case of TIBS- and F8-NODIPS-Pn, the nanoparticle powder X-ray diffractograms match very well the crystalline powder X-ray diffractogram. In the case of Br2-TIPS-Pn, there is a new peak indicating the presence of an additional polymorph. The predicted powder X-ray diffractogram of the 2,9- (rather than the 2,10-) dibromo Pn derivative was plotted for clarity. The presence of these isomers could explain the discrepancy between the experimentally obtained nanoparticle powder diffractogram and the diffractogram of the isomerically pure single crystal.

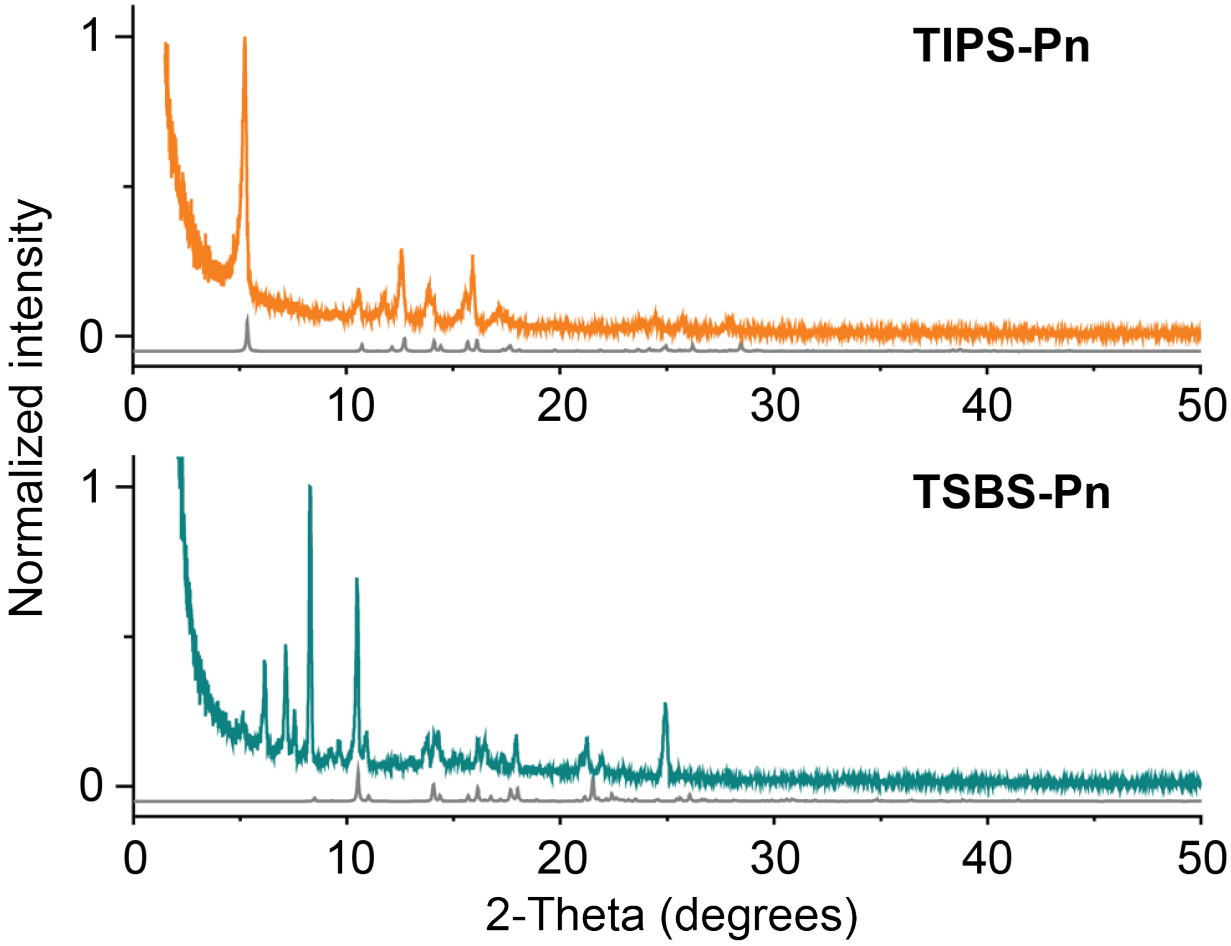

Figure S18. TIPS- and TSBS-pentacene measured nanoparticle powder and predicted powder X-ray diffractograms. The measured TIPS- and TSBS-Pn nanoparticle powder X-ray diffractograms are in orange and cyan, respectively, while the corresponding predicted powder X-ray diffractogram is depicted in grey. The preparation conditions likely induce crystallinity in the nanoparticle powders.

Pn Derivative	Molecular Packing Distances			
	Molec. Pair	π stacking (Å)	short-axis slip (Å)	long-axis slip (Å)
TIBS	1	3.1	5.0	0.2
TIPS	1	3.4	1.8	9.5
	2	3.3	0.9	6.7
F8-NODIPS	1	3.3	1.4	9.9
	2	3.3	0.9	7.5
2,9-Br2-TIPS	1	3.3	1.5	9.9
	2	3.3	1.0	7.7
2,10-Br2-TIPS	1	3.4	1.1	8.5
	2	3.4	1.1	7.8

Table S4. Packing Distances of Molecular Pairs in TIBS-, TIPS-, F8-NODIPS, and Br2-TIPS-pentacene Single Crystals. Crystallographic data were visualized using Mercury[S25] and exported into GaussView[S26] for measurement of packing distances between unique molecular pairs.

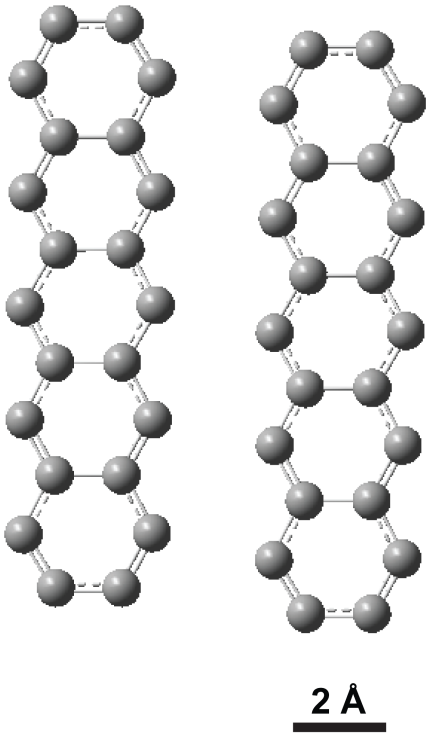

Figure S19. Stacking pattern of two TIBS-pentacene molecules projected down the normal to the pentacene plane. These data were obtained from the single crystal X-ray data. Note the extensive displacement along the short axis between the pair of molecules and seeming absence of π-stacking. Hydrogen atoms and side chains have been omitted for clarity.

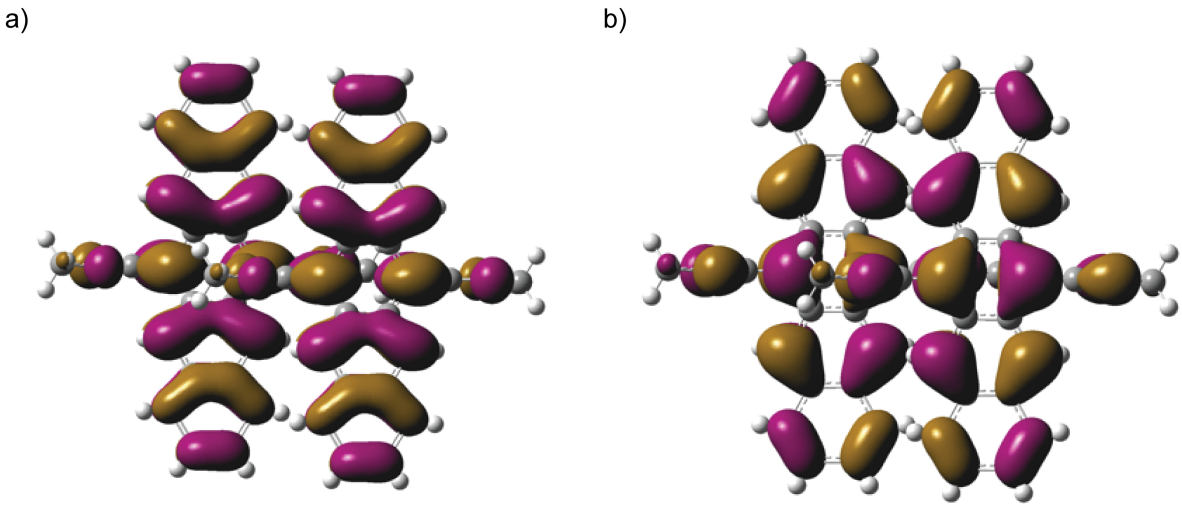

Figure S20. Results of the Hartree-Fock calculation depicting the overlap of highest occupied molecular orbitals and lowest unoccupied molecular orbitals for a pair of functionalized pentacenes. Overlap of highest occupied molecular orbitals (left panel) and lowest unoccupied molecular orbitals (right panel) for a pair of functionalized pentacenes. As can be observed from the figure above, the alkyne group overlaps with the π aromatic group of the adjacent pentacene core giving rise to orbital overlap between the two pentacene derivatives.

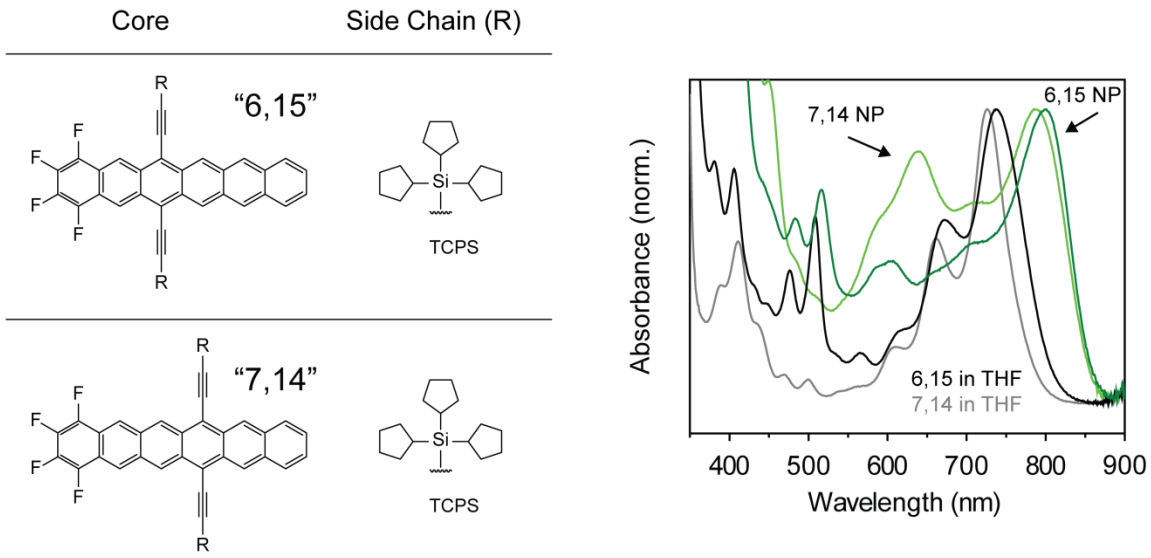

Figure S21. Halogenated hexacene derivatives and their nanoparticles. Core structure and side chains (including acronyms) of the halogenated hexacene derivatives (left panel). Steady-state absorption spectra of the hexacene derivatives in THF and their corresponding aqueous colloidal nanoparticles (right panel).

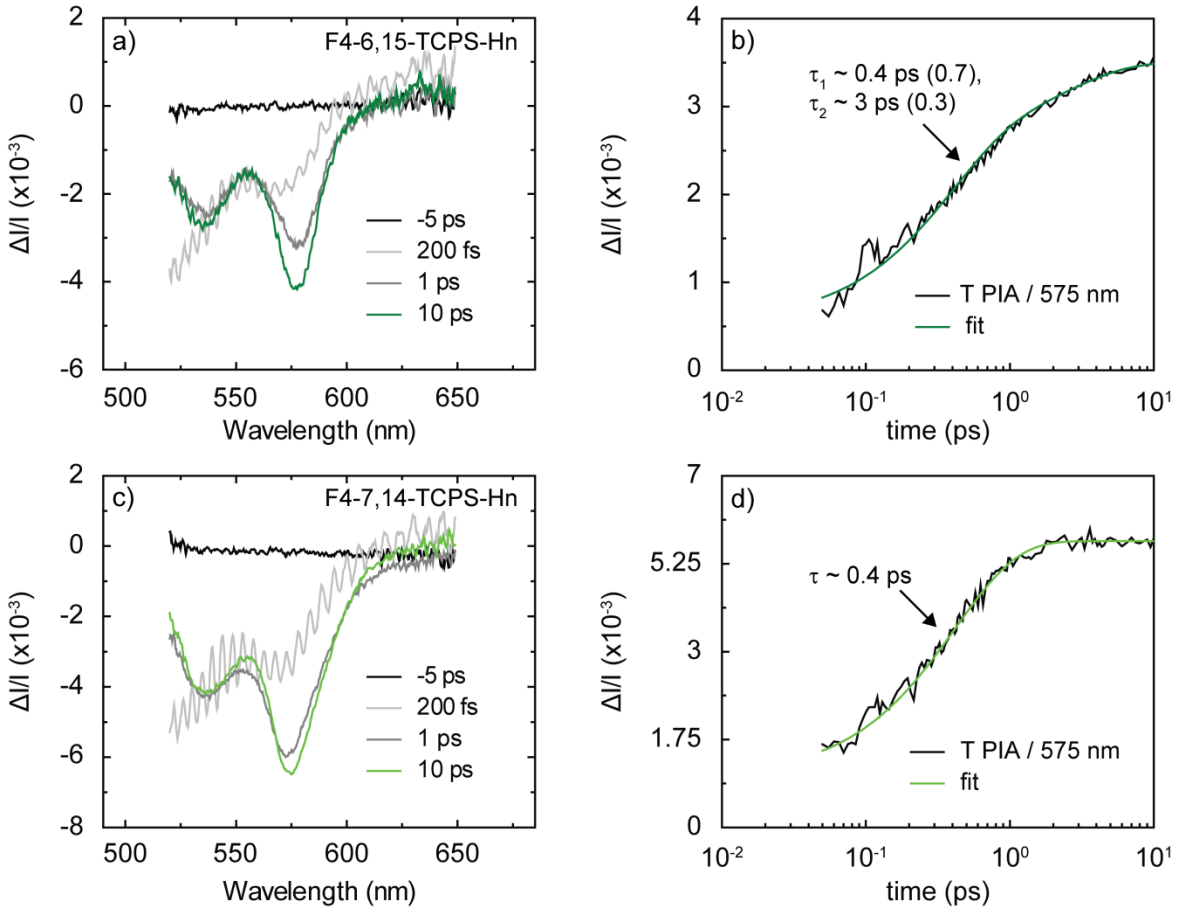

Figure S22. Pump–probe measurements on aqueous colloidal nanoparticle suspensions of halogenated hexacene derivatives. Transient absorption (a,c) spectra and (b,d) kinetics of nanoparticles of 6,15-F4-TCPS-Hn (top panels) and 7,14-F4-TCPS-Hn (bottom panels). The broad, relatively unstructured transient spectrum measured at early pump–probe time delay (c.f. 200 fs) exhibits a PIA peaking at short wavelengths along with the more structured transient spectra measured at later pump–probe time delays (c.f. 1 and 10 ps) that exhibit PIA peaks at ca. 575 and 530 nm. These transient spectra are consistent with the singlet and triplet transient spectra, respectively, reported previously for a polycrystalline hexacene film[S17] and a film of an alkyne-substituted hexacene derivative[S27] that undergo singlet fission. The transient kinetics were analyzed at the peak of the triplet PIA at ca. 575 nm. The 6,15-F4-TCPS-Hn nanoparticle triplet

transient kinetics were best described by a bi-exponential fit with time constants of ca. 0.4 and 3 ps and corresponding amplitudes of 0.7 and 0.3, respectively. The 7,14-F4-TCPS-Hn nanoparticle triplet transient kinetics were suitably described by a single exponential fit with a time constant of ca. 0.4 ps. These experiments were carried out on samples with an average optical density of ~0.006 or less in the vicinity of the NOPA spectrum and with an incident pump fluence of ~1 mJ/cm^2 (corresponding to an absorbed pump fluence of approximately ~14 μJ/cm^2 or less).

References (SI):

S1. Purushothaman, B.; Parkin, S. R.; Kendrick, M. J.; David, D.; Ward, J. W.; Yu, L.; Stingelin, N.; Jurchescu, O. D.; Ostroverkhova, O.; Anthony, J. E. *Chem. Commun.* **2012**, *48*, 8261–8263.

S2. Mooney, J.; Kambhampati, P. *J. Phys. Chem. Lett.* **2013**, *4*, 3316–3318.

S3. Rurack, K.; Spieles, M. *Anal. Chem.* **2011**, *83*, 1232–1242.

S4. Gaussian 09, Revision D.01, Frisch, M. J.; Trucks, G. W.; Schlegel, H. B.; Scuseria, G. E.; Robb, M. A.; Cheeseman, J. R.; Scalmani, G.; Barone, V.; Mennucci, B.; Petersson, G. A.; Nakatsuji, H.; Caricato, M.; Li, X.; Hratchian, H. P.; Izmaylov, A. F.; Bloino, J.; Zheng, G.; Sonnenberg, J. L.; Hada, M.; Ehara, M.; Toyota, K.; Fukuda, R.; Hasegawa, J.; Ishida, M.; Nakajima, T.; Honda, Y.; Kitao, O.; Nakai, H.; Vreven, T.; Montgomery, J. A., Jr.; Peralta, J. E.; Ogliaro, F.; Bearpark, M.; Heyd, J. J.; Brothers, E.; Kudin, K. N.; Staroverov, V. N.; Kobayashi, R.; Normand, J.; Raghavachari, K.; Rendell, A.; Burant, J. C.; Iyengar, S. S.; Tomasi, J.; Cossi, M.; Rega, N.; Millam, M. J.; Klene, M.; Knox, J. E.; Cross, J. B.; Bakken, V.; Adamo, C.; Jaramillo, J.; Gomperts, R.; Stratmann, R. E.; Yazyev, O.; Austin, A. J.; Cammi, R.; Pomelli, C.; Ochterski, J. W.; Martin, R. L.; Morokuma, K.; Zakrzewski, V. G.; Voth, G. A.; Salvador, P.; Dannenberg, J. J.; Dapprich, S.; Daniels, A. D.; Farkas, Ö.; Foresman, J. B.; Ortiz, J. V.; Cioslowski, J.; Fox, D. J. Gaussian, Inc., Wallingford CT, 2009.

S5. Becke, A. D. *J. Chem. Phys.* **1993**, *98*, 5648–5652.

S6. Stephens, P. J.; Devlin, F. J.; Chabalowski, C. F.; Frisch, M. J. *J. Phys. Chem.* **1994**, *98*, 11623–11627.

S7. Petersson, G. A.; Al-Laham, M. A. *J. Chem. Phys.* **1991**, *94*, 6081–6090.

S8. Foresman, J. B.; Head-Gordon, M.; Pople, J. A.; Frisch, M. J. *J. Phys. Chem.* **1992**, *96*, 135–149.

S9. Klimov, V. I.; Mikhailovsky, A. A.; McBranch, D. W.; Leatherdale, C. A.; Bawendi, M. G. *Science* **2000**, *287*, 1011–1013.

S10. Cassette, E.; Pensack, R. D.; Mahler, B.; Scholes, G. D. *Nat. Commun.* **2015**, *6*, 6086.

S11. Anthony, J. E.; Brooks, J. S.; Eaton, D. L.; Parkin, S. R. *J. Am. Chem. Soc.* **2001**, *123*, 9482–9483.

S12. Lunt, R. R.; Giebink, N. C.; Belak, A. A.; Benziger, J. B.; Forrest, S. R. *J. Appl. Phys.* **2009**, *105*, 053711.

S13. Luhman, W. A.; Holmes, R. J. *Adv. Funct. Mater.* **2011**, *21*, 764–771.

S14. Johnson, J. C.; Nozik, A. J.; Michl, J. *Acc. Chem. Res.* **2013**, *46*, 1290–1299.

S15. Schrauben, J. N.; Ryerson, J. L.; Michl, J.; Johnson, J. C. *J. Am. Chem. Soc.* **2014**, *136*, 7363–7373.

S16. Yost, S. R.; Lee, J.; Wilson, M. W. B.; Wu, T.; McMahon, D. P.; Parkhurst, R. R.; Thompson, N. J.; Congreve, D. N.; Rao, A.; Johnson, K.; Sfeir, M.Y.; Bawendi, M.G.; Swager, T.M.; Friend, R.H.; Baldo, M.A.; Van Voorhis, T. *Nat. Chem.* **2014**, *6*, 492–497.

S17. Busby, E.; Berkelbach, T. C.; Kumar, B.; Chernikov, A.; Zhong, Y.; Hlaing, H.; Zhu, X.-Y.; Heinz, T. F.; Hybertsen, M. S.; Sfeir, M. Y.; Reichman, D.R.; Nuckolls, C.; Yaffe, O. *J. Am. Chem. Soc.* **2014**, *136*, 10654–10660.

S18. Smith, M. B.; Michl, J. *Chem. Rev.* **2010**, *110*, 6891–6936.

S19. Roberts, S. T.; McAnally, R. E.; Mastron, J. N.; Webber, D. H.; Whited, M. T.; Brutchey, R. L.; Thompson, M. E.; Bradforth, S. E. *J. Am. Chem. Soc.* **2012**, *134*, 6388–6400.

S20. Dillon, R. J.; Piland, G. B.; Bardeen, C. J. *J. Am. Chem. Soc.* **2013**, *135*, 17278–17281.

S21. Herz, J.; Buckup, T.; Paulus, F.; Engelhart, J.; Bunz, U. H. F.; Motzkus, M. *J. Phys. Chem. Lett.* **2014**, *5*, 2425–2430.

S22. Wu, Y.; Liu, K.; Liu, H.; Zhang, Y.; Zhang, H.; Yao, J.; Fu, H. *J. Phys. Chem. Lett.* **2014**, *5*, 3451–3455.

S23. Ramanan, C.; Smeigh, A. L.; Anthony, J. E.; Marks, T. J.; Wasielewski, M. R. *J. Am. Chem. Soc.* **2012**, *134*, 386–397.

S24. Lakowicz, J. R. *Principles of Fluorescence Spectroscopy*; Springer: New York, 2006.

S25. *Mercury* version 3.3; The Cambridge Crystallographic Data Centre: Cambridge, United Kingdom, 2013.

S26. *GaussView* version 5; Gaussian, Inc.: Wallingford, Connecticut, 2009.

S27. Lee, J.; Bruzek, M. J.; Thompson, N. J.; Sfeir, M. Y.; Anthony, J. E.; Baldo, M. A. *Adv. Mater.* **2013**, *25*, 1445–1448.

Full citation for refs. 14, 20, 24, 29, 30, and 38 (main text)

14. Jadhav, P. J.; Brown, P. R.; Thompson, N.; Wunsch, B.; Mohanty, A.; Yost, S. R.; Hontz, E.; Van Voorhis, T.; Bawendi, M. G.; Bulović, V.; Baldo, M.A. *Adv. Mater.* **2012**, *24*, 6169–6174.

20. Thompson, N. J.; Wilson, M. W. B.; Congreve, D. N.; Brown, P. R.; Scherer, J. M.; Bischof, T. S.; Wu, M.; Geva, N.; Welborn, M.; Voorhis, T. V.; Bulovoć, V.; Bawendi, M.G.; Baldo, M.A. *Nat. Mater.* **2014**, *13*, 1039–1043.

24. Busby, E.; Berkelbach, T. C.; Kumar, B.; Chernikov, A.; Zhong, Y.; Hlaing, H.; Zhu, X.-Y.; Heinz, T. F.; Hybertsen, M. S.; Sfeir, M. Y.; Reichman, D.R.; Nuckolls, C.; Yaffe, O. *J. Am. Chem. Soc.* **2014**, *136*, 10654–10660.

29. Eaton, S. W.; Shoer, L. E.; Karlen, S. D.; Dyar, S. M.; Margulies, E. A.; Veldkamp, B. S.; Ramanan, C.; Hartzler, D. A.; Savikhin, S.; Marks, T. J.; Wasielewski, M.R. *J. Am. Chem. Soc.* **2013**, *135*, 14701–14712.

30. Yost, S. R.; Lee, J.; Wilson, M. W. B.; Wu, T.; McMahon, D. P.; Parkhurst, R. R.; Thompson, N. J.; Congreve, D. N.; Rao, A.; Johnson, K.; Sfeir, M.Y.; Bawendi, M.G.; Swager, T.M.; Friend, R.H.; Baldo, M.A.; Van Voorhis, T. *Nat. Chem.* **2014**, *6*, 492–497.

38. Johnson, J. C.; Akdag, A.; Zamadar, M.; Chen, X.; Schwerin, A. F.; Paci, I.; Smith, M. B.; Havlas, Z.; Miller, J. R.; Ratner, M. A.; Nozik, A.J.; Michl, J. *J. Phys. Chem. B* **2013**, *117*, 4680–4695.